



Sylvestre, M. A. S., Teanby, N. A., Dobrijevic, M., Sharkey, J., & Irwin, P. G. J. (2020). C₂N₂ vertical profile in Titan's stratosphere. *Astronomical Journal*, 160(4), [178]. <https://doi.org/10.3847/1538-3881/abafb2>

Peer reviewed version

Link to published version (if available):
[10.3847/1538-3881/abafb2](https://doi.org/10.3847/1538-3881/abafb2)

[Link to publication record in Explore Bristol Research](#)
PDF-document

This is the author accepted manuscript (AAM). The final published version (version of record) is available online via IOP Publishing at <https://doi.org/10.3847/1538-3881/abafb2> . Please refer to any applicable terms of use of the publisher.

University of Bristol - Explore Bristol Research

General rights

This document is made available in accordance with publisher policies. Please cite only the published version using the reference above. Full terms of use are available: <http://www.bristol.ac.uk/red/research-policy/pure/user-guides/ebr-terms/>

C₂N₂ vertical profile in Titan's stratosphere

M. SYLVESTRE,¹ N. A. TEANBY,¹ M. DOBRIJEVIC,² J. SHARKEY,¹ AND P. G. J. IRWIN³

¹*School of Earth Sciences, University of Bristol, Wills Memorial Building, Queens Road, Bristol BS8 1 RJ, UK*

²*Laboratoire d'astrophysique de Bordeaux, Univ. Bordeaux, CNRS, B18N, allée Geoffroy Saint-Hilaire, 33615 Pessac, France*

³*Atmospheric, Oceanic, & Planetary Physics, Department of Physics, University of Oxford, Clarendon Laboratory, Parks Road, Oxford OX1 3PU, UK*

Submitted to Astronomical Journal

ABSTRACT

In this paper, we present the first measurements of the vertical distribution of cyanogen (C₂N₂) in Titan's lower atmosphere at different latitudes and seasons, using Cassini/CIRS far-IR data. We also study the vertical distribution of three other minor species detected in our data: methylacetylene (C₃H₄), diacetylene (C₄H₂) and H₂O, in order to compare them to C₂N₂, but also to get an overview of their seasonal and meridional variations in Titan's lower stratosphere from 85 km to 225 km. We measured an average volume mixing ratio of C₂N₂ of $6.2 \pm 0.8 \times 10^{-11}$ at 125 km at the equator, but poles exhibit a strong enrichment in C₂N₂ (up to a factor 100 compared to the equator), greater than what was measured for C₃H₄ or C₄H₂. Measuring C₂N₂ profiles provides constraints on the processes controlling its distribution, such as bombardment by Galactic Cosmic Rays which seem to have a smaller influence on C₂N₂ than predicted by photochemical models.

1. INTRODUCTION

Titan's atmosphere is mainly composed of N₂ (98%) and CH₄ (between 1% and 1.5% in the stratosphere, in [Lellouch et al. 2014](#); [Bézard 2014](#); [Niemann et al. 2010](#)), but also hosts a large variety of trace gases. Hydrocarbons and nitriles (C_xH_yN_z) such as C₂H₂ and HCN are produced by the dissociation of the two main atmospheric components by solar UV and EUV photons, Saturn's magnetospheric electrons and Galactic Cosmic Rays (GCR), and by the subsequent reactions between the different species

produced ([Vuitton et al. 2019](#)). The oxygen bearing species CO, CO₂ and H₂O were also detected (e.g [Lutz et al. 1983](#); [Samuelson et al. 1983](#); [Coustenis et al. 1998](#)) although the origin of the oxygen is not fully understood. Different sources such as Enceladean plumes or micrometeorite ablation have been proposed (e.g in [Hörst et al. 2008](#); [Dobrijevic et al. 2014](#)). Characterizing the spatial distribution of Titan's trace gases and their temporal variations allow us to better understand the chemical and dynamical processes of its atmosphere and how they are affected by the seasonal variations of insolation caused by Titan's obliquity (26.7°). The data from the Cassini mission have been particularly helpful as they provided a monitor-

ing of Titan’s atmosphere from 2004 to 2017,
i.e. from northern winter to summer solstice
(Nixon et al. 2019).

In this paper, we focus on C_2N_2 (cyanogen)
as its distribution in Titan’s atmosphere is not
very well constrained. Cui et al. (2009) used
Cassini/INMS data and measured an abun-
dance of C_2N_2 of $4.8 \pm 0.8 \times 10^{-5}$ in the ther-
mosphere (1077 km). In the stratosphere, the
meridional distribution of C_2N_2 and its seasonal
evolution around 85 km have been studied with
Cassini/CIRS (Sylvestre et al. 2018; Teanby
et al. 2009) and previously with Voyager I/IRIS
(Coustenis & Bezard 1995). However, the verti-
cal distribution of C_2N_2 has only been measured
once at $70^\circ N$ in 1980 (during northern spring),
by Coustenis et al. (1991) using Voyager I/IRIS.
This polar profile is not directly comparable
with photochemical models, which typically use
low latitudes or equatorial conditions.

In the present study, we measured C_2N_2 ver-
tical profiles in Titan’s stratosphere, using
Cassini/CIRS data to cover different latitudes
and seasons. We compared the C_2N_2 verti-
cal distribution and its seasonal evolution with
other species present in our data such as C_3H_4 ,
 C_4H_2 and H_2O to better understand the atmo-
spheric processes at play in Titan’s atmosphere.

2. DATA ANALYSIS

2.1. Observations

We used observations from the thermal in-
frared spectrometer Cassini/CIRS (Composite
InfraRed Spectrometer, Flasar et al. 2004; Jen-
nings et al. 2017; Nixon et al. 2019). CIRS
is composed of three focal planes operating
at different wavenumbers: $10 - 600 \text{ cm}^{-1}$
($17 - 1000 \text{ }\mu\text{m}$) for FP1, $600 - 1100 \text{ cm}^{-1}$
($9 - 17 \text{ }\mu\text{m}$) for FP3, and $1100 - 1400 \text{ cm}^{-1}$
($7 - 9 \text{ }\mu\text{m}$) for FP4.

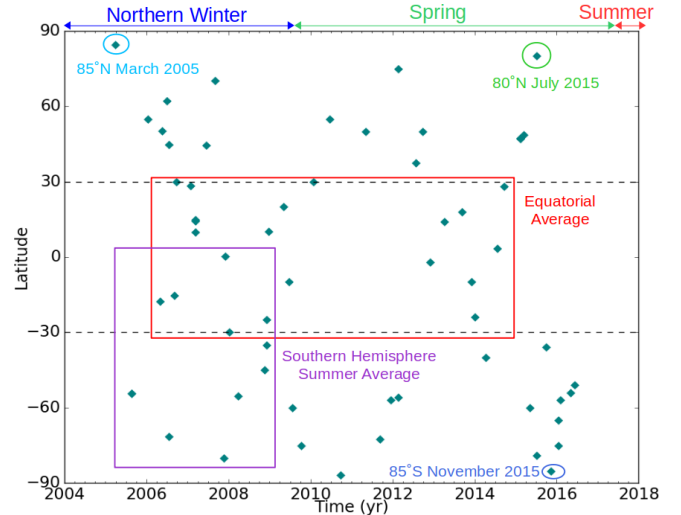


Figure 1. Spatial and temporal distribution of the limb datasets presented in this paper. Teal diamonds represent the available Cassini/CIRS limb data. Spatial averages indicated with rectangles.

In this study, we analysed limb (line of sight
perpendicular to the local vertical) and nadir
(line of sight toward the centre of Titan) FP1
spectra in the $200 - 350 \text{ cm}^{-1}$ range, with a
spectral resolution of 0.5 cm^{-1} and a sampling
interval of 0.25 cm^{-1} . During the limb observa-
tions, spectra are measured at 125 km and 225
km of altitude. The response of the FP1 de-
tector can be represented by a Gaussian with a
50% integrated response diameter of 2.54 mrad,
truncated at a radius $r = 1.95 \text{ mrad}$ from the
centre of the field of view (Teanby & Irwin
2007; Flasar et al. 2004), which corresponds to
a vertical field of view of 70 km on average. For
each altitude, an acquisition lasts from 10 to
30 minutes, which allows recording of 7 to 45
spectra, which are averaged together to increase
the S/N by a factor \sqrt{N} (with N the number
of spectra). Nadir observations are realised in
”sit-and-stare” geometry where the detector
probes the same latitude and longitude during
the acquisition, with an average field of view
of 20° of latitude. For each observation, 100
to 330 spectra were acquired over a 1.5 - 4.5
hour period. These spectra were then averaged

117 together.

118

119 Figure 1 shows the spatial and temporal dis-
 120 tribution of all the available FP1 limb obser-
 121 vations with a spectral resolution of 0.5 cm^{-1} .
 122 In most datasets (datasets not acquired pole-
 123 ward from 60°S in autumn winter, or poleward
 124 from 60°N at all seasons), the C_2N_2 band at
 125 234 cm^{-1} (see fig. 2) was too weak to enable
 126 the retrieval of the molecule’s vertical profile.
 127 That is why we chose to focus on a few spe-
 128 cific datasets, representative of different seasons
 129 and latitudes and grouped other more equato-
 130 rial datasets together to improve the signal to
 131 noise. We measured the vertical distribution of
 132 C_2N_2 at 85°N in 2005 (during northern winter),
 133 at 80°N in 2015 (during northern spring), at
 134 85°S in 2015 (during southern autumn), and
 135 we averaged all the spectra measured in the
 136 southern hemisphere between 2005 and 2009
 137 during southern summer, and in the equatorial
 138 area (30°N - 30°S) over the duration of the mis-
 139 sion. These averages will be later respectively
 140 designated as ”southern hemisphere summer
 141 average” and ”equatorial average”. For each
 142 of them, a preliminary inspection of the in-
 143 cluded datasets showed weak variations of radi-
 144 ances in the C_2N_2 band for similar temperatures
 145 (e.g Mathé et al. 2019; Sylvestre et al. 2019).
 146 **This suggested that strong variations of**
 147 **C_2N_2 were not present within these av-**
 148 **erages.** Effects of the averages on retrieved
 149 abundances were assessed by comparing our
 150 results for C_4H_2 and C_3H_4 with previous non-
 151 averaged CIRS observations at similar times
 152 and latitudes (see Section 3.1). For each case,
 153 we associate limb and nadir spectra measured
 154 at similar epoch (within a year) and latitude
 155 (within 5°), to obtain measurements at three
 156 different altitudes (225 km and 125 km with the
 157 limb observations, 85 km with the nadir obser-
 158 vations) and probe Titan’s lower stratosphere.
 159 The datasets presented in this study are listed

160 in Tables 1 and 2.

161

162 2.2. Retrieval method

163 Figure 2 shows examples of limb spectra in the
 164 $200 - 350 \text{ cm}^{-1}$ range. We measure the abun-
 165 dance of C_2N_2 using its ν_5 band at 234 cm^{-1} .
 166 Other spectral features are visible such as the ν_9
 167 band of C_4H_2 at 220 cm^{-1} , ν_{10} band of C_3H_4 at
 168 327 cm^{-1} , and several absorption bands of H_2O ,
 169 for instance at 202 cm^{-1} , 208 cm^{-1} , 228 cm^{-1} ,
 170 and 254 cm^{-1} . We retrieve the abundances
 171 of these gases using the constrained non-linear
 172 inversion code NEMESIS (Irwin et al. 2008).
 173 NEMESIS uses an iterative algorithm where
 174 a synthetic spectrum is calculated from a ref-
 175 erence atmosphere and *a priori* values for the
 176 retrieved parameters. For each iteration, these
 177 values are updated to minimise the difference
 178 between the measured and the synthetic spec-
 179 tra, until convergence is reached and the im-
 180 provement in misfit is less than 0.1%.

181

182 We adopt the same reference atmosphere
 183 as Sylvestre et al. (2018) which takes into
 184 account the abundances of the main con-
 185 stituents of Titan’s atmosphere, as measured
 186 by Cassini/CIRS, Cassini/VIMS, ALMA , and
 187 Huygens/GCMS. The composition of this ref-
 188 erence atmosphere and the relevant references
 189 are fully detailed in Sylvestre et al. (2018).

190

191 Aerosol properties and vertical distributions
 192 are derived from previous Cassini/CIRS mea-
 193 surements of de Kok et al. (2007, 2010); Vinatier
 194 et al. (2012), with the four types of hazes de-
 195 scribed in de Kok et al. (2007): hazes 0 (70 cm^{-1}
 196 to 400 cm^{-1}), A (centred at 140 cm^{-1}), B (cen-
 197 tred at 220 cm^{-1}) and C (centred at 190 cm^{-1}).

198

199 Spectroscopic parameters are the same as in
 200 Sylvestre et al. (2018), except for the Col-
 201 lision Induced Absorption coefficients (CIA).
 202 We adopted the model presented in Bézard

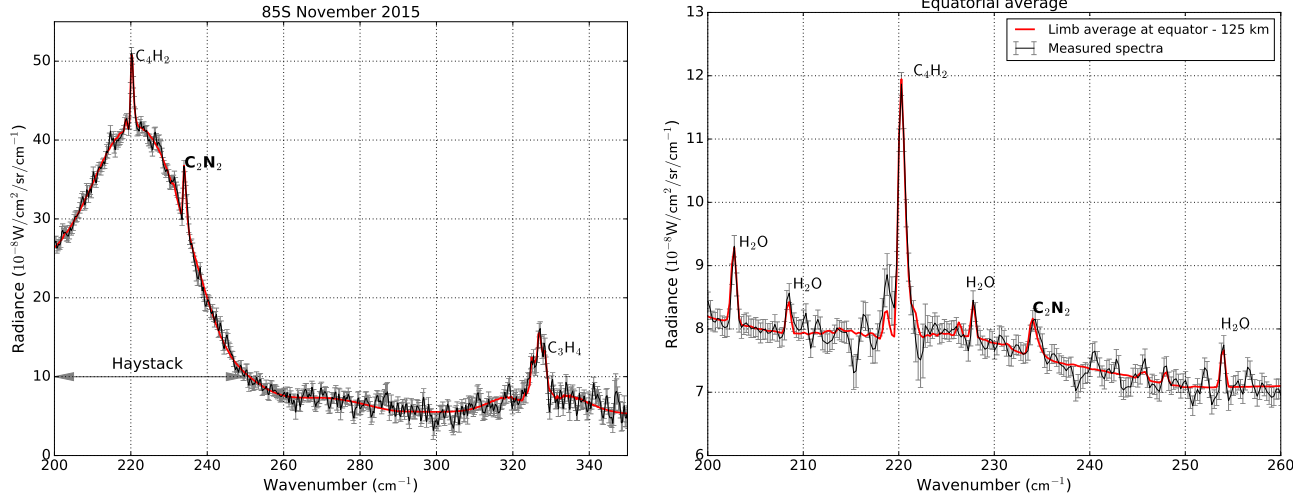


Figure 2. Examples of spectra measured with Cassini/CIRS (black lines) and matching synthetic spectra calculated by NEMESIS (red lines). The spectral resolution is 0.5 cm^{-1} ; data points are spaced by 0.25 cm^{-1} . *Left panel:* Limb spectrum measured at 85°S in November 2015 at 125 km. Note the presence of the haystack feature, which is visible only in limb and nadir far-IR spectra measured at high latitudes (poleward from 60°) in autumn and winter. H_2O bands are not visible at high latitudes. *Right panel:* Average of all the limb spectra measured at 125 km between 30°N and 30°S over the duration of the Cassini mission (later referenced as "equatorial average"), with a close-up on the $200\text{--}260 \text{ cm}^{-1}$ region where C_2N_2 , C_4H_2 and H_2O bands are visible.

& Vinatier (2019), where the coefficients for the $\text{N}_2 - \text{CH}_4$ CIA from Borysow & Tang (1993) and the $\text{N}_2 - \text{N}_2$ CIA from Borysow & Frommhold (1986a) are multiplied by the following factors:

$$C_{\text{N}_2-\text{CH}_4} = 1 + \frac{0.5}{(T - T_{\text{sat}})^2 + 1} \quad (1)$$

$$C_{\text{N}_2-\text{N}_2} = 2^{\frac{\sigma-110}{2.5 \times T-100}} \quad (2)$$

where T , T_{sat} and σ are respectively local temperature, CH_4 saturation temperature and wavenumber. Coefficients for $\text{H}_2 - \text{N}_2$ and $\text{CH}_4 - \text{CH}_4$ CIA remain the same as in Borysow & Frommhold (1986b, 1987).

For each of the cases presented in figure 1, limb and nadir spectra were fitted individually as follow:

Southern summer hemisphere average and 80°N in July 2015—For each limb spectrum, we retrieved scale factors toward the nominal profiles of C_2N_2 , C_3H_4 , C_4H_2 , H_2O , and the four types of hazes previously defined. The effect of

the large field of view of the CIRS FP1 limb data was taken into account by dividing their field of view into M parts, generating synthetic spectra for each of these parts, and using a weighted average of these spectra, as described in Teanby & Irwin (2007). We chose $M = 11$ so that the errors in the modelled radiance stay smaller than the measurement noise. We set the temperature profiles for the considered latitudes and dates using previous Cassini/CIRS measurements of Sylvestre et al. (2019) and Teanby et al. (2019). For each gas, we used the abundances retrieved from the two limb spectra (at 125 km and 225 km) to build *a priori* profiles for the nadir retrievals. We then retrieved C_2N_2 , C_3H_4 , C_4H_2 , and H_2O scale factors from the nadir spectra using these *a priori* profiles. We also retrieved simultaneously scale factors for hazes 0, B, and C and a temperature profile (as the tropospheric temperature contributes to the continuum emission of the nadir spectra).

85°N in March 2005 and 85°S in November 2015

—The previous method had to be adapted to these datasets, in order to fit the haystack feature (see fig. 2) in both limb and nadir spectra. We retrieved the cross-sections of haze B for each spectrum while keeping the vertical distribution measured in de Kok et al. (2007). We also retrieve simultaneously scale factors for C₂N₂, C₃H₄, C₄H₂, H₂O and haze 0 profiles, and a temperature profile (only for the nadir spectra).

Equatorial average—We follow a method similar as in the first case, except that this time, it was necessary to fit new cross-sections for haze 0 in each limb spectrum while scale factors were retrieved for hazes B and C. This difference could be due to the fact that the equatorial average was made by averaging CIRS spectra over 8 years, unlike the other datasets where spectra were measured at a single date or over a half a season (2005-2009 for the southern hemisphere summer average).

Errors due to measurement noise, forward modelling and smoothing of the profiles by NEMESIS and are on the order of 10% on average. For the equatorial average, as we used an average temperature profile as *a priori*, we assess the effects of temperature variations on the considered latitude and time range by retrieving these datasets using the coldest and warmest temperature profiles measured at the equator over the Cassini mission. We found that the errors due to temperature variations are also about 10%.

For each dataset, the level of detection of a gas can be assessed by calculating the change in the misfit $\Delta\chi^2$, defined as:

$$\Delta\chi^2 = \chi^2 - \chi_0^2 \quad (3)$$

with:

$$\chi^2 = \sum_{i=1}^N \frac{(I_{mes}(w_i) - I_{fit}(w_i, x))^2}{2\sigma_i^2} \quad (4)$$

where I_{mes} and I_{fit} are respectively the measured and fitted radiance, at a given wavenumber w_i and for a value x of the abundance of the considered gas. σ_i is the measurement error at w_i . The factor 2 at the denominator is to calculate the χ^2 for the correct number of independent points, as spectra have a sampling interval of 0.25 cm⁻¹ while their spectral resolution is 0.5 cm⁻¹. χ_0^2 is the value of χ^2 with $x = 0$. In the datasets presented here, C₄H₂ and C₃H₄ were always detected at more than 3- σ ($\Delta\chi^2 \leq -9$). When C₂N₂ and H₂O were not detected at 3 σ , we looked for their 3- σ upper limits, i.e. the value x for which $\Delta\chi^2 = 9$. This was especially relevant at the poles, where water could not be detected at more than 1- σ , and for C₂N₂ which could not be detected at the equator at 225 km.

Figure 3 shows the normalized contribution functions for C₄H₂ (at 220.25 cm⁻¹), C₂N₂ (at 234 cm⁻¹), C₃H₄ (at 326.75 cm⁻¹), and H₂O (at 202 cm⁻¹). Taking into account their field of view, the combination of limb and nadir data are sensitive in the 75-265 km altitude range for C₂N₂, C₄H₂ and C₃H₄, and in the 90-265 km range for H₂O. C₂N₂ and C₃H₄ contribution functions are similar for the equatorial average and 85°S in 2015. However, the cold polar temperatures of southern autumn increase the altitude at which C₄H₂ condenses, shift the contribution function of the nadir spectra upwards (from 85 km to 95 km), and make the contribution function of the limb spectrum at 125 km narrower.

3. RESULTS AND DISCUSSIONS

3.1. C₃H₄ and C₄H₂

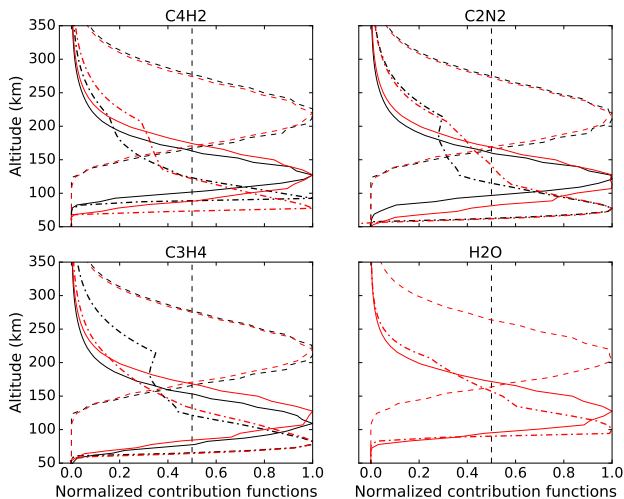


Figure 3. Normalized contribution functions for the equatorial average (in red) and 85°S in November 2015 (in black). Solid and dashed lines represent respectively the contribution functions for the limb data at 125 km and 225 km. Dot-dashed lines stand for nadir data. The combination of the limb and nadir FP1 data allows to measure C_2N_2 , C_3H_4 , C_4H_2 in the 75–265 km range, and H_2O between 90 km and 245 km. Note that the contribution functions of the equatorial average and for 85°S in November 2015 are often very similar (and hence superimposed), except for the C_4H_2 nadir and 125 km limb spectra, as the cold polar temperatures shift the C_4H_2 condensation level upward.

In figure 4 we present the results of our limb and nadir measurements for C_3H_4 , C_4H_2 , C_2N_2 , and H_2O .

We show our measurements of C_3H_4 in panel (a) and C_4H_2 in panel (b). With our equatorial limb and nadir spectral averages over the Cassini mission, we obtained profiles of C_4H_2 and C_3H_4 that are increasing with altitude (from $1.1 \pm 0.05 \times 10^{-9}$ at 85 km to $4.1 \pm_{0.3}^{0.4} \times 10^{-9}$ at 225 km for C_4H_2 , and from $3.7 \pm 0.1 \times 10^{-9}$ at 85 km to $6.9 \pm_{0.6}^{0.9} \times 10^{-9}$ at 225 km for C_3H_4). Previous Cassini/CIRS studies showed that below 300 km, at the equator, trace gases abundances vary weakly throughout the Cassini mission (e.g Mathé et al. 2019;

Teanby et al. 2019). The volume mixing ratios retrieved from our equatorial spectral average should thus be comparable to previous individual measurements at specific times during the Cassini mission. For instance fig. 4 shows that our profiles of C_4H_2 are in very good agreement with the results of Mathé et al. (2019) with Cassini/CIRS FP3 measurements at 0°N in March 2009, while we measured slightly smaller abundances than them for C_3H_4 . Lombardo et al. (2019a) averaged Cassini/CIRS FP3 limb spectra acquired between 20°S and 20°N from 2004-2009 and found a nearly constant with altitude volume mixing ratio of 1×10^{-8} between 110 km and 400 km, which is also slightly larger than our results. These differences can be explained by the characteristics of the compared datasets, especially the different vertical coverages and resolutions (10 to 50 km for the limb data of Mathé et al. 2019; Lombardo et al. 2019a), the use of detectors operating in different wavelengths and thus the use of different spectroscopic data. Our results are also consistent with the nadir CIRS FP3 measurements from Coustenis et al. (2019) who measured volume mixing ratios of $4.9 \pm 1 \times 10^{-9}$ for C_3H_4 and $1.1 \pm 0.3 \times 10^{-9}$ for C_4H_2 at 10 mbar (100 km) at the equator in 2017, and nadir measurements of Teanby et al. (2019) who found average abundances of 9×10^{-9} for C_3H_4 and 2×10^{-9} at 1 mbar (180 km) at the equator throughout the Cassini mission.

We observe a similar situation when comparing the C_3H_4 and C_4H_2 profiles measured from our limb and nadir spectral averages over the southern hemisphere in summer (2005-2009) with: Mathé et al. (2019) at 46°S in December 2007, the measurements of Coustenis et al. (2019) and Teanby et al. (2019), and the average profile of C_3H_4 in the southern hemisphere measured by Lombardo et al. (2019a) in 2004-2009 (20°S-60°S). Besides, Coustenis

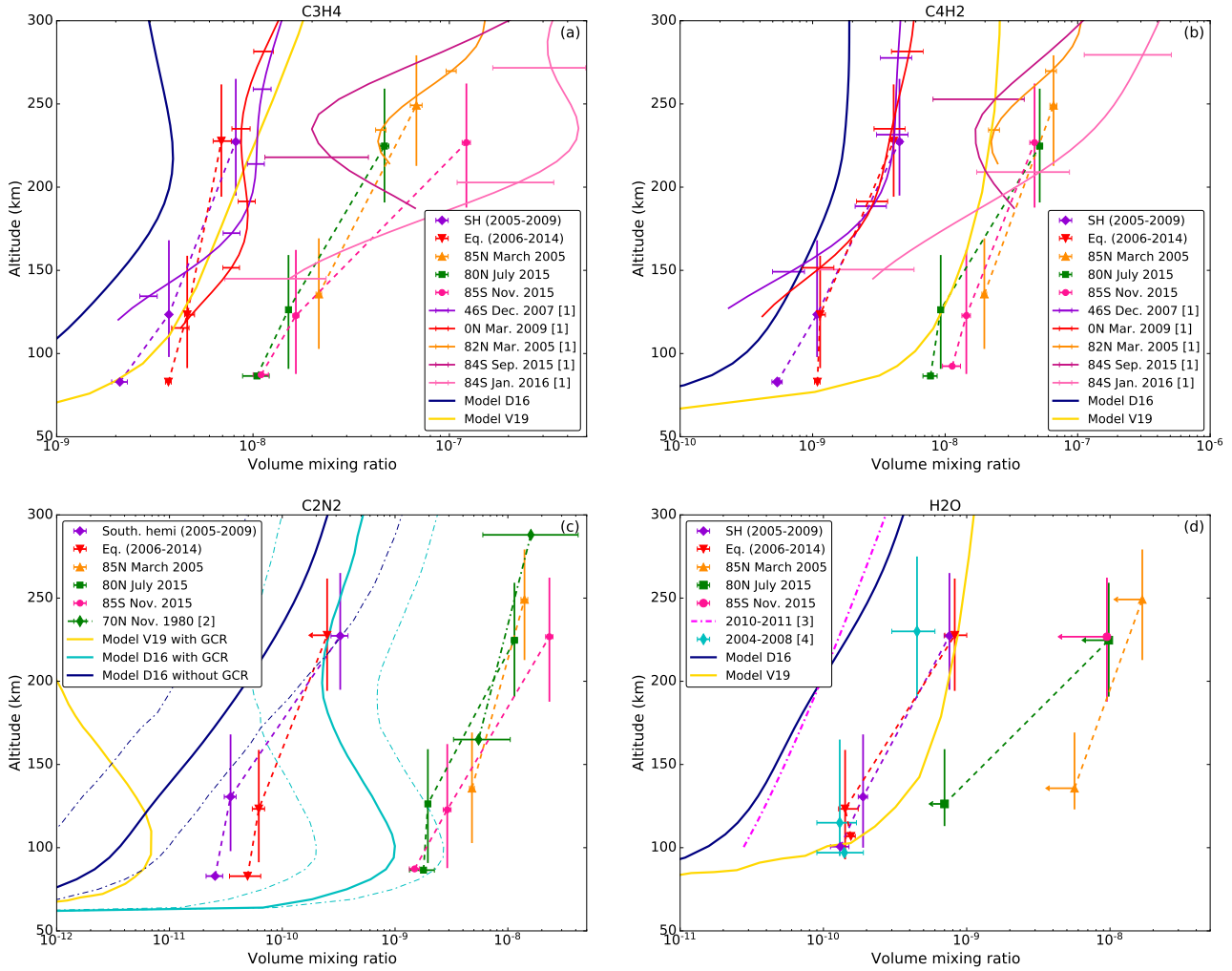


Figure 4. Vertical profiles of C_3H_4 , C_4H_2 , C_2N_2 , and H_2O . Markers indicate the volume mixing ratios measured from limb and nadir measurements. Vertical lines represent the field of view of the limb data. Dashed lines help to visualize the vertical variations of these 4 species. V19 and D16 stand respectively for the nominal photochemical model predictions of [Vuitton et al. \(2019\)](#) and [Dobrijevic et al. \(2016\)](#); [Loison et al. \(2019\)](#). *Panels (a) and (b):* [1] indicates the Cassini/CIRS limb measurements of [Mathé et al. \(2019\)](#). *Panels (c) and (d):* [2], [3] and [4] are respectively the measurements of [Coustenis et al. \(1991\)](#) with Voyager 1/IRIS, [Moreno et al. \(2012\)](#) with Herschel/PACS and HIFI, and [Cottini et al. \(2012\)](#) with Cassini/CIRS. In panel (c), the uncertainties around the profiles of model D16 are shown for C_2N_2 as thin dot-dashed lines.

et al. (2019); [Mathé et al. \(2019\)](#); [Teanby et al. \(2019\)](#) showed that trace gas abundances remain fairly constant below 300 km throughout southern summer. Consequently our equatorial and summer southern hemisphere averages seem to capture fairly well the composition of Titan's atmosphere in the lower atmosphere, despite the large latitude and time ranges used.

Besides, using nadir FP1 data allows us to probe lower altitudes (down to 85 km) than the studies cited above, and thus to complete them with information about the lower part of the stratosphere, as shown in [Sylvestre et al. \(2018\)](#); [Lombardo et al. \(2019b\)](#). For instance, fig. 4 shows that in summer, abundances of C_3H_4 and C_4H_2 in the southern

hemisphere are smaller than at the equator at 85 km (by a factor 2 for C_4H_2), while they are similar for both latitudes above 125 km and up to 360 km for C_3H_4 and 440 km for C_4H_2 . When compared to photochemical models predictions, the C_3H_4 profile measured at the equator is in good agreement with the predictions of Vuitton et al. (2019) (model V19 on fig. 4). The model of Dobrijevic et al. (2016); Loison et al. (2019) (model D16 on fig. 4) underestimates the abundance of this gas by up to a factor 10 at 85 km. The abundances predicted by Dobrijevic et al. (2016); Loison et al. (2019) for C_4H_2 are also smaller than the abundances we measured at the equator (by up to a factor 10) at 85 km. The nominal model of Vuitton et al. (2019) overestimates by a factor 10 C_4H_2 abundances, but their model without H heterogeneous loss (loss of hydrogen atoms when they interact with the surface of aerosols) is in very good agreement with our CIRS measurements. This is consistent with what Mathé et al. (2019) noted with their own CIRS observations at higher altitudes.

At high latitudes, we measure an enrichment in C_3H_4 and C_4H_2 compared to the equator (by a factor 17 for C_3H_4 and 10 for C_4H_2 at $85^\circ S$ in November 2015 at 225 km). This is in good agreement with the results from previous studies (e.g. Coustenis et al. 2019; Mathé et al. 2019; Teanby et al. 2019), especially if we take into account the strong dynamical activity and rapid evolution of the poles, for instance when the South Pole goes from autumn to winter solstice, as illustrated by the differences between the profiles measured at $84^\circ S$ in September 2015 and January 2016 by Mathé et al. (2019) (see fig. 4), and as described by Teanby et al. (2017). This is due to the atmospheric circulation that evolves from 2 equator-to-poles cells at the equinox, to a single pole-to-pole cell with a strong subsidence above the autumn/winter pole that advects photochemical products from

their production area in the upper atmosphere to the lower atmosphere, as shown in Titan's **General Circulation Models** (GCM, Vatan d'Ollone et al., *in prep*, Vatan d'Ollone et al. 2017; Lebonnois et al. 2012; Lora et al. 2015; Newman et al. 2011). At high northern latitudes, C_3H_4 and C_4H_2 abundances have decreased slightly from March 2005 to July 2015 i.e. from winter to late spring. This confirms previous observations of Sylvestre et al. (2018) (at 85 km) and Mathé et al. (2019) (in the 175-280 km altitude range) where the enrichment in photochemical species at the North pole persists up to January 2015 in the lower stratosphere, whereas a depletion is observed in the upper stratosphere from December 2011 (Vinatier et al. 2015; Mathé et al. 2019). These observations are consistent with the persistence of a small circulation cell above the high northern latitudes during the transition from the two equator-to-poles cells to a single pole-to-pole during most of the northern spring as predicted by the LMDZ GCM (Vatan d'Ollone et al. 2017; Lebonnois et al. 2012) (see also figure 12 of Sylvestre et al. (2018)). In July 2015, this residual circulation cell has disappeared, thus allowing the depletion in trace gases of the lower stratosphere by upwelling.

3.2. C_2N_2

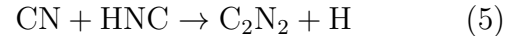
Panel (c) of fig. 4 shows the C_2N_2 profiles we measured at different latitudes and seasons. At the equator, we measured an average profile over the Cassini mission where C_2N_2 increases from $5.0 \pm 1.5 \times 10^{-11}$ at 85 km to $6.2 \pm 0.8 \times 10^{-11}$ at 125 km, and a $3 - \sigma$ upper limit of 2.5×10^{-10} at 225 km. In the southern hemisphere in summer (2005-2009) we were able to measure an abundance of $6.8 \pm 0.6 \times 10^{-10}$ for C_2N_2 at 225 km. The C_2N_2 abundances retrieved from **the southern summer dataset** below 225 km are smaller than the abundances at the equator, similar to what was measured

for C_4H_2 and C_3H_4 . The LMDZ GCM predicts that during northern winter the upwelling due to the ascending branch of the pole-to-pole cell is the strongest above southern mid-latitudes. Air depleted in photochemical products (due to their condensation) is thus advected upward in the southern hemisphere, which explains why it has lower C_2N_2 , C_3H_4 , and C_4H_2 than at the equator.

At high latitudes, our measurements are consistent with the profile at $70^\circ N$ by Coustenis et al. (1991). C_2N_2 profiles exhibit a strong enrichment compared to our equatorial or southern hemisphere summer averages. This trend is similar to the measurements of C_2N_2 at 15 mbar (85 km) by Sylvestre et al. (2018), and to what has been measured for C_3H_4 and C_4H_2 . The seasonal evolution of C_2N_2 at high northern latitudes is also very similar to the evolution of C_4H_2 and C_3H_4 , with a slight decrease from northern winter (2005) to late spring (2015). The enrichment in C_2N_2 at the poles is much larger than the enrichment in C_3H_4 and C_4H_2 . For instance, in our results, $85^\circ S$ in 2015, the C_2N_2 volume mixing ratio at 225 km was at least 100 times larger than at the equator, whereas C_3H_4 and C_4H_2 abundances were respectively 17 and 10 times larger than at the equator. This is consistent with the results of Teanby et al. (2010) where nitriles were more enriched than hydrocarbons with similar photochemical lifetimes, which could indicate the presence of an additional loss process for nitriles.

In fig. 4, the CIRS profiles of C_2N_2 are compared with the profiles predicted by the photochemical models of Vuitton et al. (2019) (Model V19 in fig. 4) and of Dobrijevic et al. (2016); Loison et al. (2015) (Model D16 in fig. 4). The abundances we measured at the equator and in the southern hemisphere in summer are the

same order of magnitude as the predictions of Dobrijevic et al. (2016) and 1-2 orders of magnitude larger than the results of Vuitton et al. (2019). This may be explained by the different chemical reaction schemes of these two models, and more particularly in the main production reactions for C_2N_2 , which for Vuitton et al. (2019) is:



and for Dobrijevic et al. (2016) is:



which is not taken into account into the model of Vuitton et al. (2019). However, significant uncertainties remain about the kinetics of reaction 6 (V. Vuitton, personal communication). In both models, the main loss reaction in the lower stratosphere is:



unlike the photochemical model of Krasnopol'sky (2014), where C_2N_2 is mainly lost by photodissociation and where the C_2N_2 abundance is overestimated by a factor 60.

Galactic Cosmic Rays (GCR) ionize N_2 in the lower stratosphere with a magnitude comparable to solar UV in the upper atmosphere (Gronoff et al. 2009), hence creating a second production region for C_2N_2 at lower altitude in photochemical models. In Vuitton et al. (2019) and Dobrijevic et al. (2016), instead of increasing with altitude like C_4H_2 abundance, C_2N_2 profile exhibits a local maximum between 100 km and 200 km (see fig. 4). Below 100 km, C_2N_2 abundance decreases with decreasing altitude as this gas reacts with other species and condenses. When we compare the profiles of C_2N_2 from Dobrijevic et al. (2016) with and without GCR, our measurements at the equator and in the southern hemisphere in summer are

in good agreement with the profile with GCR at 225 km, but not in agreement with either profiles below 125 km, where photochemical models predict a local maximum of C_2N_2 due to the GCR. This seems to indicate a smaller influence of the GCR on C_2N_2 profile than predicted by the models. However, their effect can not be completely ruled out as we do not observe the steep decrease with pressure predicted without GCR.

Many other nitrogen-bearing species are predicted to be affected by the GCR bombardment. For instance, in Dobrijevic et al. (2016), HNC is predicted to be up to 100 times more abundant below 600 km when effects of GCR bombardment are included. However, recent ALMA measurements of the vertical profile of HNC are in better agreement with the predictions of Dobrijevic et al. (2016) without the effects of GCR (Lellouch et al. 2019). GCR may also have a strong effect on the $^{14}\text{N}/^{15}\text{N}$ ratios in $\text{C}_2\text{H}_5\text{CN}$ and CH_3CN , as they could be up to twice as high as in HCN or HC_3N (Dobrijevic & Loison 2018). Iino et al. (2020) ALMA measurements of $^{14}\text{N}/^{15}\text{N}$ in CH_3CN were not inconsistent with these predictions, but not precise enough to be conclusive. The production of amines (e.g NH_3 , CH_3NH_2 , CH_3NHCH_3), imines (e.g CH_2NH), and aromatics could also be increased by the GCR (by up to 3 orders of magnitude for amines and imines, Loison et al. 2015, 2019), but observational data are insufficient for these species.

3.3. H_2O

Panel (d) of fig. 4 presents our measurements for the H_2O abundances. At the equator, the abundance of water increases with altitude from $1.6 \pm 0.1 \times 10^{-10}$ at 100 km to $8.2 \pm_{1.2}^{1.8} \times 10^{-10}$ at 225 km. In the lower atmosphere, our results are consistent with the Cassini/CIRS measurements of Cottini et al. (2012) (see fig. 4) and of Bauduin et al. (2018), and about one order of magnitude larger than the Herschel mea-

surements of Moreno et al. (2012). Bauduin et al. (2018) explained the inconsistency between the CIRS and Herschel results by potential meridional and seasonal variations in H_2O abundance. At 225 km, we measured a H_2O abundance twice as large as Cottini et al. (2012). In the southern hemisphere in summer, H_2O abundance is within error bars from the equatorial measurements at all probed altitudes unlike C_3H_4 , C_4H_2 and C_2N_2 for which volume mixing ratios are significantly smaller in the southern hemisphere than at the equator below 125 km. This difference of behaviour is expected as H_2O is predicted to have a much longer lifetime than C_3H_4 , C_4H_2 , and C_2N_2 . At the poles, we could only measure $3 - \sigma$ upper limits of H_2O which allow us to say that autumn/winter poles can not be enriched in water by more than a factor 10 compared to the equator at 225 km. These results are not inconsistent with the meridional and seasonal variations in water distribution suggested by Bauduin et al. (2018) to explain the differences between the Cassini/CIRS and the Herschel results.

Our H_2O profiles are also compared to the photochemical models of Dobrijevic et al. (2016); Loison et al. (2019) (Model D16 in fig. 4) and Vuitton et al. (2019) (Model V19 in fig. 4). The profile from Vuitton et al. (2019) is in good agreement with our measurements at the equator and **in the southern hemisphere in summer** whereas the predictions of Dobrijevic et al. (2016); Loison et al. (2019) are one order of magnitude smaller than our results. As Dobrijevic et al. (2016) used the results of Moreno et al. (2012) to constrain the eddy diffusion coefficient in their model, the good agreement between these two studies is expected. More measurements of H_2O abundance are required to constrain further its variations and understand the processes that shape its vertical and

meridional distribution.

4. CONCLUSION

In this paper, we present the first study of the C_2N_2 vertical distribution for different latitudes and seasons in Titan’s stratosphere, using Cassini/CIRS measurements. At the equator we measured a C_2N_2 abundance increasing with altitude, from $5.0 \pm 1.5 \times 10^{-11}$ at 85 km to $6.2 \pm 0.8 \times 10^{-11}$ at 125 km and a $3\text{-}\sigma$ upper limit of 2.5×10^{-10} at 225 km. Poles are enriched in C_2N_2 , by up to a factor 100 compared to the equator. Comparing these vertical profiles with the predictions of recent photochemical models helps to constrain the chemistry of this gas, especially on the role of the Galactic Cosmic Rays that seem less important than predicted in the models. These data also allowed us to measure profiles of C_3H_4 and C_4H_2 in the lower part of the stratosphere (down to 85 km), which is usually not probed by mid-infrared Cassini/CIRS observations. We could thus extend the description of the meridional and seasonal variations

of these species to this part of Titan’s atmosphere. This study also provides insights on the variations of the H_2O abundance in Titan’s lower atmosphere, including upper limits on its potential enrichment by the atmospheric circulation at the poles (up to a factor 10).

ACKNOWLEDGMENTS

This research was funded by the UK Sciences and Technology Facilities Research council (grant number ST/R000980/1) and the Cassini project. This research made use of Astropy, a community-developed core Python package for Astronomy ([Astropy Collaboration et al. 2013](#)), and matplotlib, a Python library for publication quality graphics ([Hunter 2007](#)). We thank Jan Vasant d’Ollone for insightful discussions about the predictions of the LMDZ GCM, Véronique Vuitton for useful comments about Titan’s photochemistry, and the anonymous reviewer for their suggestions.

APPENDIX

A. ANALYSED DATASETS

Table 1. Cassini CIRS nadir datasets analysed in this study. N is the number of spectra measured during the acquisition. Asterisks denote the datasets used in the Equatorial Average. † denote the datasets used in the Southern Summer Hemisphere Average.

Dataset	Date	N	Latitude (°N)
CIRS_000TLFIRNADCMP017_PRIME†	3 Jul. 2004	13	-35.5
CIRS_003TLFIRNADCMP002_PRIME†	15 Feb. 2005	180	-18.7
CIRS_005TLFIRNADCMP002_PRIME†	31 Mar. 2005	241	-41.1
CIRS_00BTLFIRNADCMP001_PRIME	12 Dec. 2004	224	16.4
CIRS_013TLFIRNADCMP004_PRIME†	22 Aug. 2005	248	-53.7

Table 1 *continued*

Table 1 (*continued*)

Dataset	Date	N	Latitude (°N)
CIRS_019TLFIRNADCMP002_PRIME†	26 Dec. 2005	124	-0.0
CIRS_021TLFIRNADCMP002_PRIME†	27 Feb. 2006	213	-30.2
CIRS_022TLFIRNADCMP003_PRIME†*	18 Mar. 2006	401	-0.4
CIRS_023TLFIRNADCMP002_PRIME†	1 May 2006	215	-35.0
CIRS_024TLFIRNADCMP003_PRIME†*	19 May 2006	350	-15.5
CIRS_029TLFIRNADCMP003_PRIME*	23 Sep. 2006	312	9.5
CIRS_030TLFIRNADCMP002_PRIME†	10 Oct. 2006	340	-59.1
CIRS_035TLFIRNADCMP023_PRIME†	12 Dec. 2006	164	-73.3
CIRS_036TLFIRNADCMP002_PRIME†	28 Dec. 2006	136	-89.1
CIRS_037TLFIRNADCMP002_PRIME†	13 Jan. 2007	107	-70.3
CIRS_038TLFIRNADCMP002_PRIME†	29 Jan. 2007	254	-39.7
CIRS_040TLFIRNADCMP001_PRIME†	09 Mar. 2007	159	-49.2
CIRS_041TLFIRNADCMP001_PRIME†	25 Mar. 2007	2	-76.8
CIRS_042TLFIRNADCMP001_PRIME†	10 Apr 2007	103	-60.8
CIRS_043TLFIRNADCMP001_PRIME†	26 Apr 2007	263	-51.4
CIRS_044TLFIRNADCMP002_PRIME*†	13 May 2007	104	-0.5
CIRS_045TLFIRNADCMP001_PRIME†	28 May 2007	231	-22.3
CIRS_046TLFIRNADCMP001_PRIME*	13 Jun. 2007	60	17.6
CIRS_046TLFIRNADCMP002_PRIME†	14 Jun. 2007	102	-20.8
CIRS_047TLFIRNADCMP001_PRIME*	29 Jun. 2007	204	9.8
CIRS_048TLFIRNADCMP001_PRIME†	18 Jul. 2007	96	-34.8
CIRS_050TLFIRNADCMP001_PRIME†*	1 Oct. 2007	144	-10.1
CIRS_053TLFIRNADCMP001_PRIME†	04 Dec. 2007	223	-40.2
CIRS_055TLFIRNADCMP001_PRIME*	05 Jan. 2008	190	18.7
CIRS_059TLFIRNADCMP001_PRIME†	22 Feb. 2008	172	-24.9
CIRS_059TLFIRNADCMP002_PRIME*	23 Feb. 2008	98	17.1
CIRS_067TLFIRNADCMP001_PRIME†	11 May 2008	48	-59.5
CIRS_069TLFIRNADCMP001_PRIME†	27 May 2008	112	-44.6
CIRS_069TLFIRNADCMP002_PRIME*	28 May 2008	112	9.5
CIRS_095TLFIRNADCMP001_PRIME†*	05 Dec. 2008	213	-14.0
CIRS_097TLFIRNADCMP001_PRIME†*	20 Dec. 2008	231	-10.9
CIRS_106TLFIRNADCMP001_PRIME†	26 Mar. 2009	165	-60.3
CIRS_110TLFIRNADCMP001_PRIME†	06 May 2009	282	-68.1
CIRS_111TLFIRNADCMP002_PRIME†	22 May 2009	168	-27.1

Table 1 *continued*

Table 1 (*continued*)

Dataset	Date	N	Latitude (°N)
CIRS_112TIFIRNADCMP002_PRIME†	7 Jun. 2009	274	-58.9
CIRS_114TIFIRNADCMP001_PRIME†	9 Jul. 2009	164	-71.4
CIRS_119TIFIRNADCMP001_PRIME†	11 Oct. 2009	5	-25.9
CIRS_119TIFIRNADCMP002_PRIME*	12 Oct. 2009	166	0.4
CIRS_123TIFIRNADCMP002_PRIME†	28 Dec. 2009	186	-46.1
CIRS_124TIFIRNADCMP002_PRIME*	13 Jan. 2010	272	-1.2
CIRS_131TIFIRNADCMP002_PRIME*	20 May 2010	229	-19.8
CIRS_133TIFIRNADCMP001_PRIME*	20 Jun. 2010	187	-49.7
CIRS_134TIFIRNADCMP001_PRIME*	06 Jul. 2010	251	-10.0
CIRS_138TIFIRNADCMP001_PRIME*	24 Sep. 2010	190	-30.1
CIRS_148TIFIRNADCMP001_PRIME*	8 May 2011	200	-10.0
CIRS_153TIFIRNADCMP001_PRIME*	11 Sep. 2011	227	9.9
CIRS_160TIFIRNADCMP002_PRIME*	30 Jan. 2012	280	-0.2
CIRS_161TIFIRNADCMP001_PRIME*	18 Feb. 2012	121	9.9
CIRS_161TIFIRNADCMP002_PRIME*	19 Feb. 2012	89	-15.0
CIRS_166TIFIRNADCMP001_PRIME*	22 May 2012	318	-19.9
CIRS_169TIFIRNADCMP001_PRIME*	24 Jul. 2012	258	-9.7
CIRS_175TIFIRNADCMP001_PRIME*	28 Nov. 2012	150	15.0
CIRS_185TIFIRNADCMP001_PRIME*	05 Apr 2013	244	15.0
CIRS_190TIFIRNADCMP001_PRIME*	23 May 2013	224	-0.2
CIRS_195TIFIRNADCMP001_PRIME*	25 Jul. 2013	186	19.6
CIRS_201TIFIRNADCMP001_PRIME*	02 Feb. 2014	329	19.9
CIRS_203TIFIRNADCMP002_PRIME*	07 Apr 2014	239	0.5
CIRS_207TIFIRNADCMP002_PRIME	21 Aug. 2014	163	79.7
CIRS_248TIFIRNADCMP001_PRIME	13 Nov. 2016	185	-88.9

REFERENCES

- 679 Astropy Collaboration, Robitaille, T. P., Tollerud,
 680 E. J., et al. 2013, A&A, 558, A33,
 681 doi: [10.1051/0004-6361/201322068](https://doi.org/10.1051/0004-6361/201322068)
 682 Bauduin, S., Irwin, P. G. J., Lellouch, E., et al.
 683 2018, Icarus, 311, 288,
 684 doi: [10.1016/j.icarus.2018.04.003](https://doi.org/10.1016/j.icarus.2018.04.003)
 685 Bézard, B. 2014, Icarus, 242, 64,
 686 doi: [10.1016/j.icarus.2014.07.013](https://doi.org/10.1016/j.icarus.2014.07.013)
 687 Borysow, A., & Frommhold, L. 1986a, ApJ, 311,
 688 1043, doi: [10.1086/164841](https://doi.org/10.1086/164841)
 689 —. 1986b, ApJ, 303, 495, doi: [10.1086/164096](https://doi.org/10.1086/164096)
 690 —. 1987, ApJ, 318, 940, doi: [10.1086/165426](https://doi.org/10.1086/165426)
 691 Borysow, A., & Tang, C. 1993, Icarus, 105, 175,
 692 doi: [10.1006/icar.1993.1117](https://doi.org/10.1006/icar.1993.1117)
 693 Bézard, B., & Vinatier, S. 2019, Icarus, doi: <https://doi.org/10.1016/j.icarus.2019.03.038>
 694

Table 2. Cassini CIRS limb datasets analysed in this study. N is the number of spectra measured during the acquisition. Asterisks denote the datasets used in the Equatorial Average. † denote the datasets used in the Southern Hemisphere Summer Average.

Dataset	Date	N	Latitude (°N)
CIRS_005TI_FIRLMBINT002_PRIME	31 Mar. 2005	26	84.6
CIRS_013TI_FIRLMBINT002_PRIME†	22 Aug. 2005	58	-54.5
CIRS_013TI_FIRLMBINT003_PRIME†	22 Aug. 2005	58	-54.5
CIRS_028TI_FIRLMBINT002_PRIME*†	7 Sep. 2006	54	-15.3
CIRS_029TI_FIRLMBINT003_PRIME*	23 Sep. 2006	70	30.0
CIRS_038TI_FIRLMBINT001_PRIME*	29 Jan. 2007	26	28.7
CIRS_040TI_FIRLMBINT001_PRIME*	9 Mar. 2007	35	9.6
CIRS_040TI_FIRLMBINT002_PRIME*	10 Mar. 2007	29	14.8
CIRS_052TI_FIRLMBINT001_PRIME†	18 Nov. 2007	24	-79.9
CIRS_053TI_FIRLMBINT001_PRIME*†	4 Dec. 2007	79	0.2
CIRS_055TI_FIRLMBINT001_PRIME*†	5 Jan. 2008	54	-29.9
CIRS_062TI_FIRLMBINT003_PRIME†	25 Mar. 2008	49	-55.3
CIRS_093TI_FIRLMBINT002_PRIME†	19 Nov. 2008	74	-44.9
CIRS_095TI_FIRLMBINT001_PRIME†	5 Dec. 2008	54	-35.1
CIRS_095TI_FIRLMBINT002_PRIME*†	5 Dec. 2008	76	-25.0
CIRS_097TI_FIRLMBINT001_PRIME*	21 Dec. 2008	55	10.1
CIRS_110TI_FIRLMBINT001_PRIME*	5 May 2009	51	20.1
CIRS_113TI_FIRLMBINT001_PRIME*†	22 Jun. 2009	59	-10.0
CIRS_115TI_FIRLMBINT002_PRIME†	24 Jul. 2009	51	-60.0
CIRS_119TI_FIRLMBINT002_PRIME†	12 Oct. 2009	60	-75.0
CIRS_125TI_FIRLMBINT001_PRIME*	28 Jan. 2010	68	29.9
CIRS_175TI_FIRLMBINT001_PRIME*	29 Nov. 2012	70	-2.0
CIRS_185TI_FIRLMBINT001_PRIME*	5 Apr. 2013	70	14.0
CIRS_200TI_FIRLMBINT002_PRIME*	1 Jan. 2014	49	-24.0
CIRS_206TI_FIRLMBINT005_PRIME*	20 Jul. 2014	65	3.5
CIRS_208TI_FIRLMBINT002_PRIME*	22 Sep. 2014	70	28.1
CIRS_218TI_FIRLMBINT001_PRIME	7 Jul. 2015	51	80.1
CIRS_225TI_FIRLMBINT002_PRIME	13 Nov. 2015	53	-84.6

695 Cottini, V., Nixon, C. A., Jennings, D. E., et al.
696 2012, *Icarus*, 220, 855,
697 doi: [10.1016/j.icarus.2012.06.014](https://doi.org/10.1016/j.icarus.2012.06.014)

698 Coustenis, A., & Bezaud, B. 1995, *Icarus*, 115,
699 126, doi: [10.1006/icar.1995.1084](https://doi.org/10.1006/icar.1995.1084)

700 Coustenis, A., Bezaud, B., Gautier, D., Marten,
701 A., & Samuelson, R. 1991, *Icarus*, 89, 152,
702 doi: [10.1016/0019-1035\(91\)90095-B](https://doi.org/10.1016/0019-1035(91)90095-B)

703 Coustenis, A., Jennings, D., Achterberg, R., et al.
704 2019, *Icarus*, 113413, doi: <https://doi.org/10.1016/j.icarus.2019.113413>
705

- Coustenis, A., Salama, A., Lellouch, E., et al. 1998, *A&A*, 336, L85
- Cui, J., Yelle, R. V., Vuitton, V., et al. 2009, *Icarus*, 200, 581, doi: [10.1016/j.icarus.2008.12.005](https://doi.org/10.1016/j.icarus.2008.12.005)
- de Kok, R., Irwin, P. G. J., Teanby, N. A., et al. 2007, *Icarus*, 191, 223, doi: [10.1016/j.icarus.2007.04.003](https://doi.org/10.1016/j.icarus.2007.04.003)
- . 2010, *Icarus*, 207, 485, doi: [10.1016/j.icarus.2009.10.021](https://doi.org/10.1016/j.icarus.2009.10.021)
- Dobrijevic, M., Hébrard, E., Loison, J. C., & Hickson, K. M. 2014, *Icarus*, 228, 324, doi: [10.1016/j.icarus.2013.10.015](https://doi.org/10.1016/j.icarus.2013.10.015)
- Dobrijevic, M., & Loison, J. C. 2018, *Icarus*, 307, 371, doi: [10.1016/j.icarus.2017.10.027](https://doi.org/10.1016/j.icarus.2017.10.027)
- Dobrijevic, M., Loison, J. C., Hickson, K. M., & Gronoff, G. 2016, *Icarus*, 268, 313, doi: [10.1016/j.icarus.2015.12.045](https://doi.org/10.1016/j.icarus.2015.12.045)
- Flasar, F. M., Kunde, V. G., Abbas, M. M., et al. 2004, *SSRv*, 115, 169, doi: [10.1007/s11214-004-1454-9](https://doi.org/10.1007/s11214-004-1454-9)
- Gronoff, G., Lilensten, J., Desorgher, L., & Flückiger, E. 2009, *A&A*, 506, 955, doi: [10.1051/0004-6361/200912371](https://doi.org/10.1051/0004-6361/200912371)
- Hörst, S. M., Vuitton, V., & Yelle, R. V. 2008, *Journal of Geophysical Research (Planets)*, 113, E10006, doi: [10.1029/2008JE003135](https://doi.org/10.1029/2008JE003135)
- Hunter, J. D. 2007, *Computing in Science & Engineering*, 9, 90, doi: [10.1109/MCSE.2007.55](https://doi.org/10.1109/MCSE.2007.55)
- Iino, T., Sagawa, H., & Tsukagoshi, T. 2020, *ApJ*, 890, 95, doi: [10.3847/1538-4357/ab66b0](https://doi.org/10.3847/1538-4357/ab66b0)
- Irwin, P. G. J., Teanby, N. A., de Kok, R., et al. 2008, *JQSRT*, 109, 1136, doi: [10.1016/j.jqsrt.2007.11.006](https://doi.org/10.1016/j.jqsrt.2007.11.006)
- Jennings, D. E., Flasar, F. M., Kunde, V. G., et al. 2017, *ApOpt*, 56, 5274, doi: [10.1364/ao.56.005274](https://doi.org/10.1364/ao.56.005274)
- Krasnopolsky, V. A. 2014, *Icarus*, 236, 83, doi: [10.1016/j.icarus.2014.03.041](https://doi.org/10.1016/j.icarus.2014.03.041)
- Lebonnois, S., Burgalat, J., Rannou, P., & Charnay, B. 2012, *Icarus*, 218, 707, doi: [10.1016/j.icarus.2011.11.032](https://doi.org/10.1016/j.icarus.2011.11.032)
- Lellouch, E., Bézard, B., Flasar, F. M., et al. 2014, *Icarus*, 231, 323, doi: [10.1016/j.icarus.2013.12.016](https://doi.org/10.1016/j.icarus.2013.12.016)
- Lellouch, E., Gurwell, M. A., Moreno, R., et al. 2019, *Nature Astronomy*, 3, 614, doi: [10.1038/s41550-019-0749-4](https://doi.org/10.1038/s41550-019-0749-4)
- Loison, J. C., Dobrijevic, M., & Hickson, K. M. 2019, *Icarus*, 329, 55, doi: [10.1016/j.icarus.2019.03.024](https://doi.org/10.1016/j.icarus.2019.03.024)
- Loison, J. C., Hébrard, E., Dobrijevic, M., et al. 2015, *Icarus*, 247, 218, doi: [10.1016/j.icarus.2014.09.039](https://doi.org/10.1016/j.icarus.2014.09.039)
- Lombardo, N. A., Nixon, C. A., Achterberg, R. K., et al. 2019a, *Icarus*, 317, 454, doi: [10.1016/j.icarus.2018.08.027](https://doi.org/10.1016/j.icarus.2018.08.027)
- Lombardo, N. A., Nixon, C. A., Sylvestre, M., et al. 2019b, *AJ*, 157, 160, doi: [10.3847/1538-3881/ab0e07](https://doi.org/10.3847/1538-3881/ab0e07)
- Lora, J. M., Lunine, J. I., & Russell, J. L. 2015, *Icarus*, 250, 516, doi: [10.1016/j.icarus.2014.12.030](https://doi.org/10.1016/j.icarus.2014.12.030)
- Lutz, B. L., de Bergh, C., & Owen, T. 1983, *Science*, 220, 1374, doi: [10.1126/science.220.4604.1374](https://doi.org/10.1126/science.220.4604.1374)
- Mathé, C., Vinatier, S., Bézard, B., et al. 2019, *Icarus*, 113547, doi: <https://doi.org/10.1016/j.icarus.2019.113547>
- Moreno, R., Lellouch, E., Lara, L. M., et al. 2012, *Icarus*, 221, 753, doi: [10.1016/j.icarus.2012.09.006](https://doi.org/10.1016/j.icarus.2012.09.006)
- Newman, C. E., Lee, C., Lian, Y., Richardson, M. I., & Toigo, A. D. 2011, *Icarus*, 213, 636, doi: [10.1016/j.icarus.2011.03.025](https://doi.org/10.1016/j.icarus.2011.03.025)
- Niemann, H. B., Atreya, S. K., Demick, J. E., et al. 2010, *Journal of Geophysical Research (Planets)*, 115, E12006, doi: [10.1029/2010JE003659](https://doi.org/10.1029/2010JE003659)
- Nixon, C. A., Ansty, T. M., Lombardo, N. A., et al. 2019, *ApJS*, 244, 14, doi: [10.3847/1538-4365/ab3799](https://doi.org/10.3847/1538-4365/ab3799)
- Samuelson, R. E., Maguire, W. C., Hanel, R. A., et al. 1983, *J. Geophys. Res.*, 88, 8709, doi: [10.1029/JA088iA11p08709](https://doi.org/10.1029/JA088iA11p08709)
- Sylvestre, M., Teanby, N., d'Ollone, J. V., et al. 2019, *Icarus*, doi: <https://doi.org/10.1016/j.icarus.2019.02.003>
- Sylvestre, M., Teanby, N. A., Vinatier, S., Lebonnois, S., & Irwin, P. G. J. 2018, *A&A*, 609, A64, doi: [10.1051/0004-6361/201630255](https://doi.org/10.1051/0004-6361/201630255)
- Teanby, N. A., & Irwin, P. G. J. 2007, *Ap&SS*, 310, 293, doi: [10.1007/s10509-007-9519-3](https://doi.org/10.1007/s10509-007-9519-3)
- Teanby, N. A., Irwin, P. G. J., de Kok, R., et al. 2009, *Icarus*, 202, 620, doi: [10.1016/j.icarus.2009.03.022](https://doi.org/10.1016/j.icarus.2009.03.022)

- 802 Teanby, N. A., Irwin, P. G. J., de Kok, R., &
803 Nixon, C. A. 2010, *Faraday Discussions*, 147,
804 51, doi: [10.1039/c001690j](https://doi.org/10.1039/c001690j)
805 Teanby, N. A., Sylvestre, M., Sharkey, J., et al.
806 2019, *Geophys. Res. Lett.*, 46, 3079,
807 doi: [10.1029/2018GL081401](https://doi.org/10.1029/2018GL081401)
808 Teanby, N. A., Bézard, B., Vinatier, S., et al.
809 2017, *Nature Communications*, 8, 1586,
810 doi: [10.1038/s41467-017-01839-z](https://doi.org/10.1038/s41467-017-01839-z)
811 Vatant d'Ollone, J., Lebonnois, S., & Guerlet, S.
812 2017, in *EGU General Assembly Conference*
813 *Abstracts*, Vol. 19, 10169
- 814 Vinatier, S., Rannou, P., Anderson, C. M., et al.
815 2012, *Icarus*, 219, 5,
816 doi: [10.1016/j.icarus.2012.02.009](https://doi.org/10.1016/j.icarus.2012.02.009)
817 Vinatier, S., Bézard, B., Lebonnois, S., et al. 2015,
818 *Icarus*, 250, 95, doi: [10.1016/j.icarus.2014.11.019](https://doi.org/10.1016/j.icarus.2014.11.019)
819 Vuitton, V., Yelle, R. V., Klippenstein, S. J.,
820 Hörst, S. M., & Lavvas, P. 2019, *Icarus*, 324,
821 120, doi: [10.1016/j.icarus.2018.06.013](https://doi.org/10.1016/j.icarus.2018.06.013)